

Aeroelastic Investigation of a Flying Wing Configuration Using Computational Fluid Dynamics

Noga Obstbaum and Daniella E.Raveh

Technion - Israel Institute of Technology, Haifa, Israel

February 2020

Abstract

The report summarizes a research study on aeroelastic flying wing configuration, A3TB, using Computational Fluid Dynamics(CFD). Euler and Navier-Stokes simulation were performed on the rigid and flexible aircraft configurations to compute the rigid and flexible aerodynamic coefficients due to angle-of-attack and deflected control surfaces. The research examined the influence of the solver, Euler or Navier-Stokes, on the result obtained. The main difference noticed is the change in the height of the boundary layer obtained, due to the low Re number that exists in the flight condition examined. It also included the effect of the elasticity in comparison to a rigid configuration in two aspects- the difference in the lift coefficient obtained, and the effect on flaps efficiency with the increase of the angle of attack. As expected, the effective angle of attack increases due to the elastic deformation, which causes higher values of lift coefficient but also damages the efficiency of the flaps, with the increase of the rigid angle of attack.

Nomenclature

C_D Drag coefficient

C_L Lift coefficient

C_{L_α} Lift curve Slope

C_{L_δ} Flap lift curve Slope

$C_{M_X}, C_{M_Y}, C_{M_Z}$ Moment coefficient in X,Y,Z direction

C_N	Normal force coefficient
C_X, C_Y, C_Z	Force coefficient in X,Y,Z direction
K_E	Generalized stiffness matrix
F	Aerodynamic force vector
F_E	Generalized aerodynamic force vector
g	Earth gravity constant
h	Altitude
L	Change of the temperature at the troposphere
M	Mach number
P	Pressure [Pa]
P_{SL}	Pressure at sea-level [Pa]
q	Dynamic pressure [Pa]
Q	physical quantities of the Navier-stokes equation [Pa]
R	Gas constant
Re	Reynolds number
T_{SL}	Temperature at sea-level [Pa]
u_E	Elastic displacements vector
V	Velocity [m/s]
X, Y	Coordinates
α	Angle of attack
α_{stall}	Angle of attack at stall
γ	Heat capacity ratio
δ	Flap deflection angle
η_f	Flaps efficiency
ξ	Mode deflection
ξ_E	Generalized coordinate
ϕ_E	Modes matrix

1 Introduction

The CFD analysis method has become more and more useful and reliable during recent years. Using both methods allows us to achieve the force applied to the configuration while updating the deformation obtained from that force, and vice versa.

In this paper, an investigation of a half flying wing, A3TB, has been performed. The investigation took part in a static aeroelasticity deformation, in low angles of attack. The topics examined were the difference between Euler and Navier-Stokes CFD methods, rigid and elastic performance, and the effect of the elastic wing on flaps efficiency.

2 Mathematical Model

An Euler/Navier-Stokes is used for the fluid dynamics computations. The flow, in general, is assumed to be compressible, viscous, and turbulent. A semidiscrete finite volume method using central differencing in space with explicit multistage time-stepping scheme is employed. A steady-state solution to the time-dependent Euler/Navier-Stokes equations is obtained by iterating in time using local time steps and implicit residual smoothing.

The analysis is made on two levels of iterative processes. The first level contains the CFD analysis for a fixed-shape configuration that, if iterated until convergence, provides the aerodynamic loads distribution on the rigid aircraft. The second iterative level introduces the structural elasticity that is combined with the aerodynamic loading to obtain the corresponding deformed shape. This level, if iterated until convergence, provides a load distribution that agrees with the shape of the elastic aircraft.

For computational efficiency, the elastic deformations corrections are introduced during the CFD solution convergence. The user defines a number of CFD iterations, after which elastic deformations are computed and applied to the CFD grid. The number of CFD iterations between two successive elastic deformation was set to be 22% of the number of iterations required for flow-field convergence. The shape is not updated after each CFD iteration to avoid excessive computations and numerical instabilities in the flow computations.

The difficulty in that process arises from the difference between the methods. While the CFD process required computational grid points on the outer body surface and external to that, the elastic analysis is performed at the internal elements of the wing, which carry the loads. Moreover, the CFD surface grid points are usually denser than the structure elements nodes. Therefore, a CFD-Structures interface has been applied.

Elastic Deflections

In order to use the scheme, a finite-element free-vibration analysis data, containing a low-frequency set of the free-free elastic vibration modes and a list of nodes of the elements, was introduced to the CFD analysis included. Data transfer happened only once, at the start of the simulation. All the elastic analysis are then computed within the CFD code.

The static aeroelastic equation is

$$[K_E]\{\xi_E\} = \{F_E\} \quad (1)$$

where $[K_E]$ is the generalized stiffness matrix, and $\{F_E\}$ is the associated generalized aerodynamic force vector. The generalized forces are obtained from summing the aerodynamic forces at the aerodynamic surface grid points according to

$$\{F_E\} = [\Phi_E]\{F\} \quad (2)$$

where $[\Phi_E]$ is the modes matrix, splined to the aerodynamic surface grid points, and $\{F\}$ is the aerodynamic force vector at the aerodynamic surface grid points.

Equation (1) is solved to obtain $\{\xi_E\}$, which is the vector of generalized displacements. In order to obtain the deformed shape, the elastic displacement vector at the aerodynamic grid points $\{u_E\}$ is calculated according to -

$$\{u_E\} = [\Phi_E]\{\xi_E\} \quad (3)$$

After the aerodynamic surface grid points have been updated according to the aeroelastic deflections, the field grid is also updated accordingly.

Flaps Deflections

The flap generator method that is used in the EZNSS code reads an input file that contains 2 coordinates of the flap hinge, a leading edge or trailing edge position of the flap and the flap deflection angle δ . A fictitious mesh is built on the wing surface and the control surface is deflected in this mesh. This mesh (deformed at the cs location) is then mapped to the CFD surface mesh using the same spline algorithm that is used for the elastic modes.

3 Test Case

Figure 1 shows the A3TB geometry. The rectangular wings are swept back in 22 deg. The wings are fitted with eight control surfaces that are used for trim, and fins for lateral stability. Reference dimensions are detailed in table 1 and table 2.

In this investigation, a half clamped wing was analyzed with symmetric boundary conditions at the root. The fins were not included in the CFD-model. The flaps are located at the trailing edge at 25% of the chord.

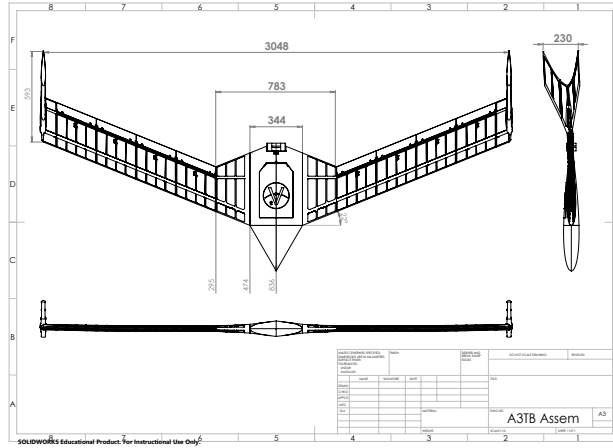


Figure 1: A3TB geometry

Table 1: A3TB Half-Configuration Dimensions

Property	Value
Reference area	$0.535(m^2)$
Reference span	$1.5(m)$
Reference chord	$0.3(m)$

Table 2: Control Surfaces Hinge Coordinates

Control surface	Root	Tip
1	$X_R = 0.626(m)$	$X_T = 0.731(m)$
	$Y_R = 0.395(m)$	$Y_T = 0.656(m)$
2	$X_R = 0.731(m)$	$X_T = 0.837(m)$
	$Y_R = 0.656(m)$	$Y_T = 0.92(m)$
3	$X_R = 0.837(m)$	$X_T = 0.942(m)$
	$Y_R = 0.92(m)$	$Y_T = 1.178(m)$
4	$X_R = 0.942(m)$	$X_T = 1.048(m)$
	$Y_R = 1.1785(m)$	$Y_T = 1.439(m)$

Grids

There are 2 types of CFD grids being used in this work. The first one is more adequate for an inviscid Euler run, and the second is more adequate to viscous Navier-Stokes run. In a viscous run, it is essential to take into account the boundary layer phenomena, and therefore the grid is much denser and has more total grid points. While in the inviscid grid there are about 2 million and a half grid points, the viscous grid has about 14 million grid points.

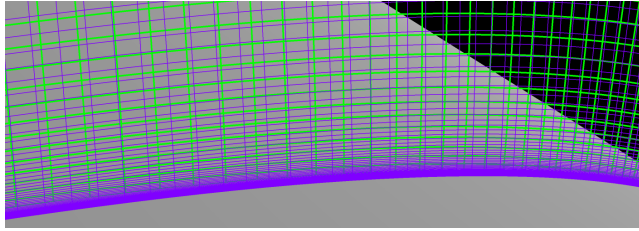


Figure 2: Grid comparison- Green-Euler grid, Purple-Navier-Stokes grid

Figure 2 display both grids around the top airfoil shape. The inviscid grid is shown in green and the viscous grid in purple. As been mention, the Navier-Stokes grid is much denser than the Euler grid.

Elastic Vibration Modes

In this work, a set of 10 low-frequency elastic vibration modes was used. The first three modes are presented in table 3 with their natural frequencies.

Figure 3 shows the first bending and Figure 4 shows the first torsion modes. In green the A3TB surface CFD grid. In blue the input spline. In red the modes deflections.

Table 3: Elastic Modes

Number of mode	Frequency [Hz]	Type
1	6.4	First symrtric mode - body pitching and wing bending
2	9.9	Second symetric mode - forward and backwards bending
3	11	Torsion

4 Results

In this section, we will provide the results from the rigid and elastic analysis. The conditions of flight are sea-level flight in the velocity of 20-30 [m/s]. At this range, the Mach number obtained is very low where the CFD code is instable.

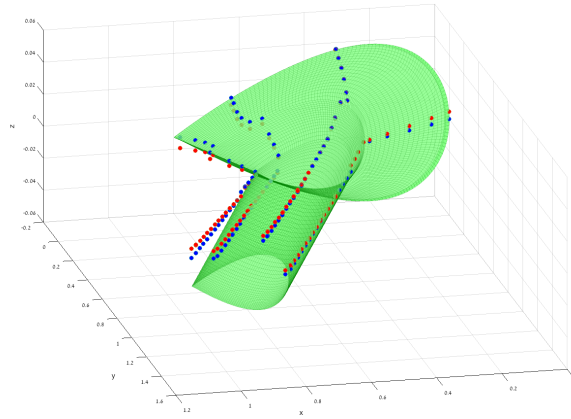


Figure 3: First bending mode

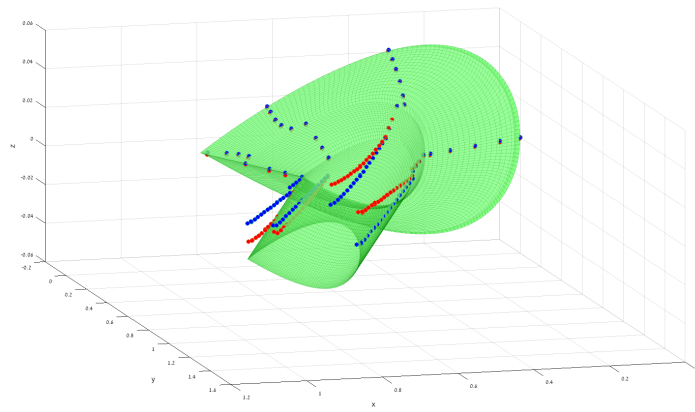


Figure 4: First torsion mode

Therefore, to achieve similar results using the computational method, we calculate the dynamic pressure and found the level of flight needed to achieve the same value, where the code is stable, at Mach number of $M=0.2$. Equations 4 and 5 used for those calculations.

$$q = \frac{1}{2}\rho V^2 = \frac{1}{2}\gamma P M^2 \quad (4)$$

$$\frac{P}{P_{SL}} = \left(1 - \frac{Lh}{T_{SL}}\right)^{\frac{\gamma}{\gamma-1}} \quad (5)$$

The EZNSS code provides the convergence result after each iteration. The convergence method used named L2NORM. The method uses equation 6 to evaluate the difference obtained from the former iteration until convergence achieved. $[\Delta Q]$ vector represent the physical quantities of the Navier-stokes equation, such as ρ , density, or $\rho \cdot u$, density multiply the x direction velocity, etc.

$$|L2NORM| = \sqrt{\sum_{k=1}^n |\Delta Q_k|^2} \quad (6)$$

4.1 Rigid Analysis - Navier-Stokes versus Euler

A comparison between an inviscid run, Euler method, and a viscous run, Navier-Stokes method, is presented.

Besides the results being shown later in the section, a significant difference between the methods is the time for a single run. Because of the difference between the CFD grids used, a single Euler iteration is much faster than one Navier-Stokes iteration. As a result, 6000 iterations in Euler method take about 6-7 hours, while 6000 iterations in the Navier-Stokes method take about 48 hours.

4.1.1 3D Analysis

Figure 5 shows lift coefficient computed for angles of attack between 0 and 5 using Euler and Navier-Stokes simulations. The values in the Euler method are a bit higher than the Navier-Stokes values. The lift curve slopes, $C_{L\alpha}$, been obtained are -

$$C_{L\alpha}^{Euler} = 4.6814 [1/\text{rad}]$$

$$C_{L\alpha}^{Navier-Stokes} = 4.2808 [1/\text{rad}]$$

The difference is 9.35%

Figure 6 shows Drag coefficient computed for these angles of attack with the two methods. As expected, there is a significant difference between the Navier-Stokes and Euler results when comparing the drag coefficient. The Euler method is inviscid, and thus does not take into consideration the boundary layer

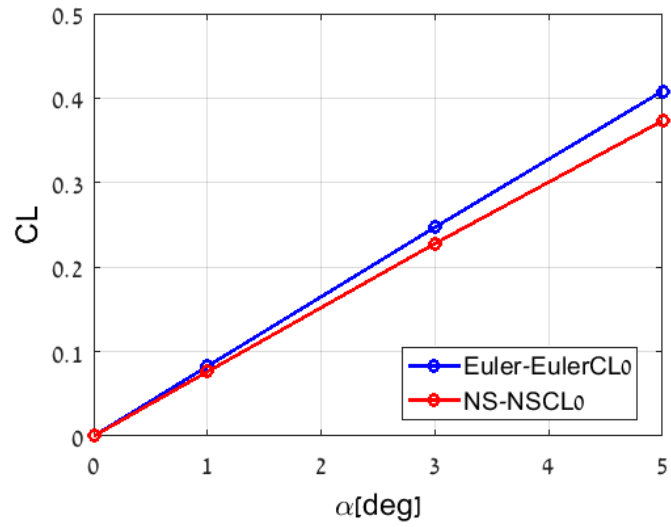


Figure 5: Lift Coefficient versus Angle of Attack, $M=0.2$, $q=226.1[\text{pa}]$, $h = 17584[m]$

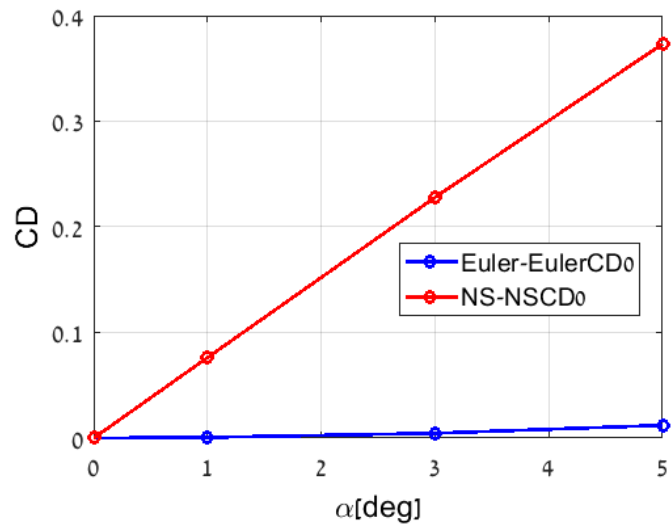


Figure 6: Drag Coefficient versus Angle of Attack, $M=0.2$, $q=226.1[\text{pa}]$, $h = 17584[m]$

phenomenon. As a result, in the Euler method we received low values of drag coefficient, while in the Navier-Stokes method, we receive realistic values.

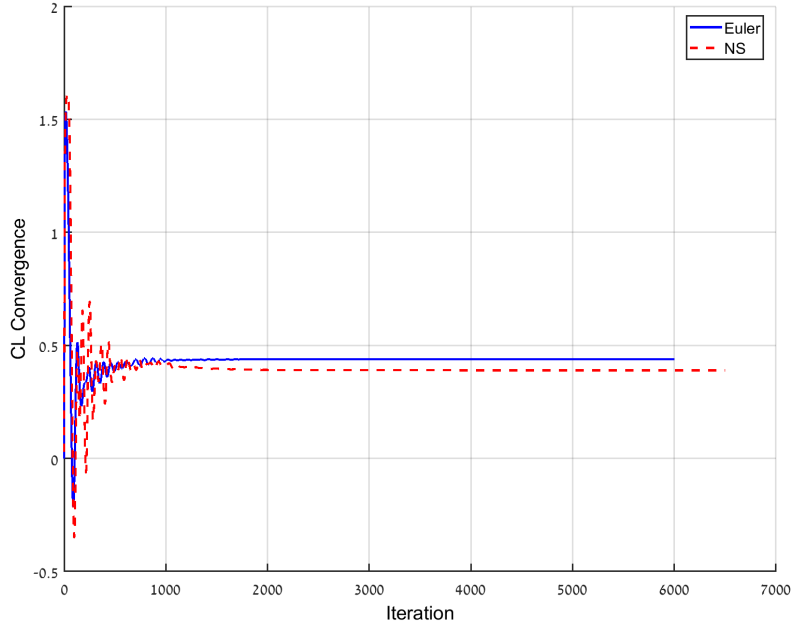


Figure 7: Lift Coefficient Convergence, $\alpha = 5^\circ$, $M=0.2$, $q=226.1[\text{pa}]$, $h = 17584[m]$

Figure 7 shows the lift coefficient convergence with the raise of the number of iterations. It appears that after 2000 iterations, the lift coefficient has converged at both methods. The Navier-Stokes curve oscillated through larger values at first, but then start to converge around the same time as the Euler method.

Figure 8 shows the L2NORM convergence method .From figure 8 we observe that both curves have almost the same behavior. The Euler curve reaches a higher value at the beginning, but also, at the end converged sooner than the Navier-Stokes curve.

4.1.2 2D NACA0012 Analysis

A possible source for the difference in the lift coefficient computed with the two methods (5) could be the Reynolds number at the analysis flight condition. At sea-level flight in velocity of 25 [m/s], we obtained $Re = \frac{1.225 \cdot 25 \cdot 0.3}{1.789 \cdot 10^{-5}} = 5.1 \cdot 10^5$.

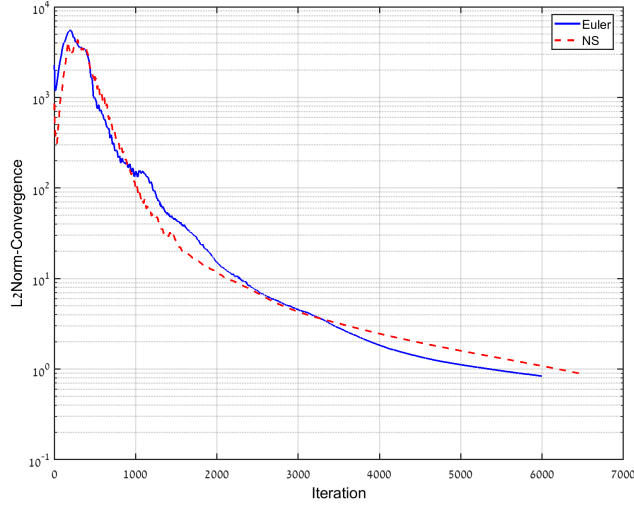


Figure 8: L2Norm Convergence, $\alpha = 5^\circ$, $M=0.2$, $q=226.1[\text{pa}]$, $h = 17584[m]$

At this low Re number, we expect to have a thick boundary layer and therefore, the significant differences between viscous and inviscid analysis.

In order to examine this hypothesis, 2D CFD runs were performed to a NACA0012 airfoil. At each run, the same flow condition were considered. The chord was varied leading to different Re numbers.

The results for sea-level standard atmosphere condition at a Mach number of 0.2 and 5° AOA, are:

type	Chord[m]	Re	CL
Euler	1	—	0.6118
	0.1	$4.66e05$	0.529
Navier-Stokes	0.5	$2.33e06$	0.546
	1	$4.66e06$	0.554
	2	$9.32e06$	0.56
	10	$4.66e07$	0.57

From table 4, as the Re number increases, at Navier-Stokes runs, the value of C_L is getting closer to value predicted by the Euler run.

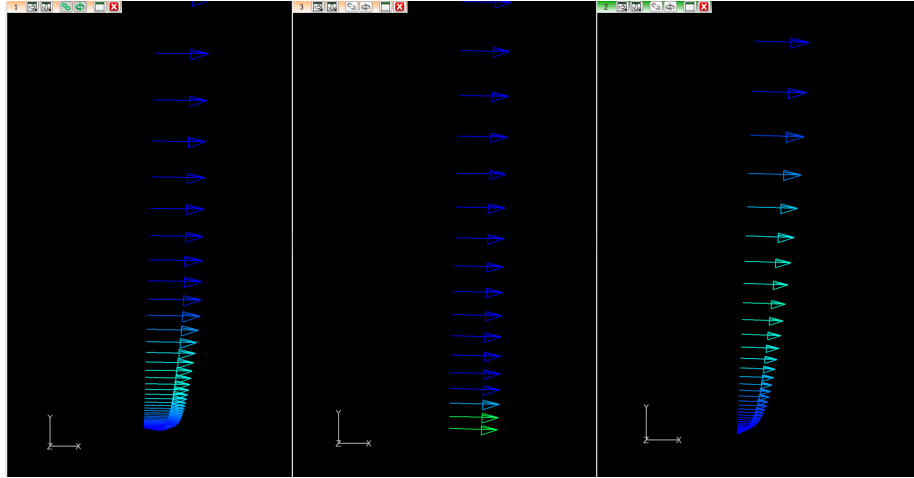


Figure 9: NACA0012 Velocity Profile

In figure 9, 3 velocity profiles show the difference in the boundary layer height. The left side is the Navier-Stokes run at $Re=1e07$, in the middle is the Euler run, and at the right side is the Navier-Stokes run at $Re=1e05$. At the Euler run, there is a small boundary layer due to numerical error. At the Navier-Stokes runs, the bigger the Re number, the smaller the boundary layer. Those differences show the effective airfoil shape. Where there is a bigger boundary layer, the effective airfoil shape is much thicker, and thus generates a lower lift coefficient value.

4.2 Elastic Analysis - Navier-Stokes

All the simulations in this section performed in the altitude of $h=14030.4$ [m], in a dynamic pressure of $q=394.8$ [pa], at Mach number of $M=0.2$, which represents the dynamic pressure at sea-level flight in the velocity of 25[m/s].

Figure 10 shows the lift coefficient computed for the flexible aircraft in several AOA values using a Navier-Stokes simulation. All of the elastic simulation computed at dynamics pressure of $394.8[Pa]$ which corresponds to 25 [m/s] at sea-level. From figure 10 we can obtain the lift line slope of the elastic configuration, the stall angle, and the maximum lift coefficient.

$$C_{L_\alpha} = 5.6875[1/rad]$$

$$\alpha_{stall} = 8^\circ$$

$$C_{L_{max}} = 0.8$$

C_{L_α} was computed for the linear region, based on lift values at 0° and 8° AOA.

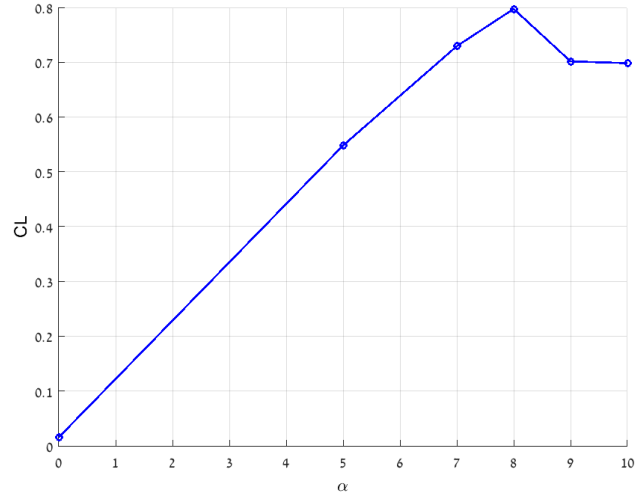


Figure 10: Lift Coefficient versus Angle of Attack, flexible configuration

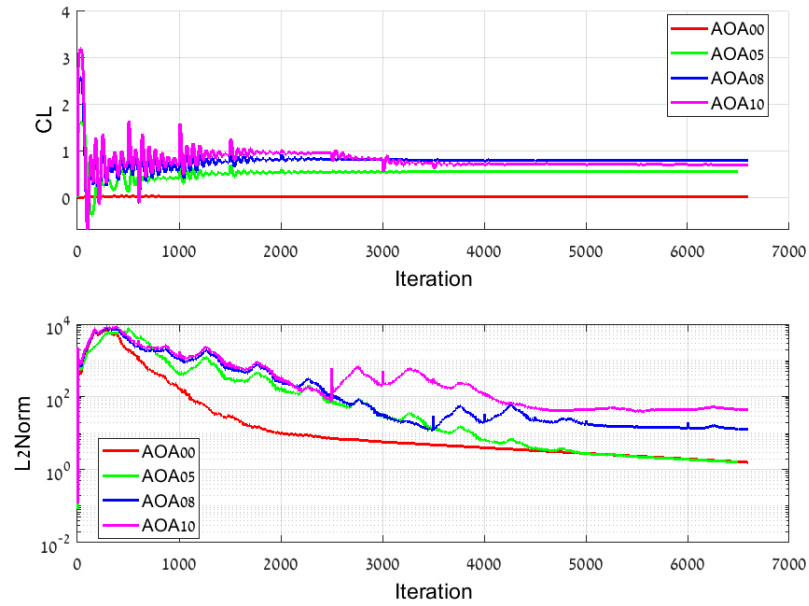
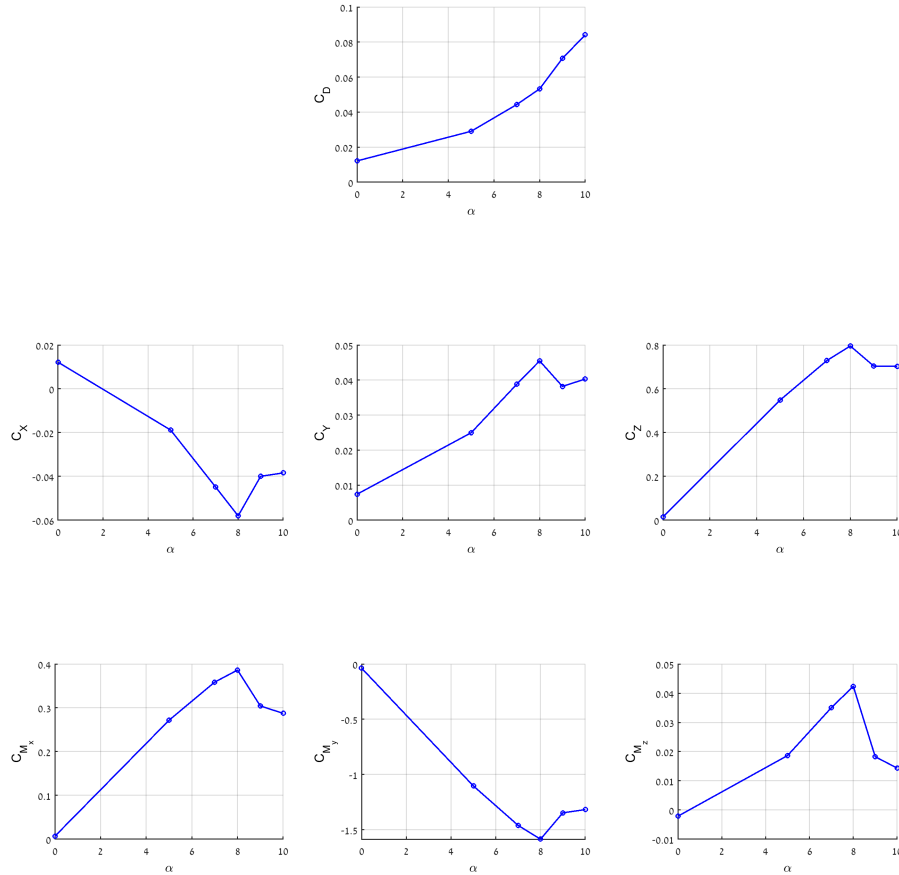


Figure 11: Navier-Stokes Convergence, flexible configuratio, $\alpha = [0^\circ, 5^\circ, 8^\circ, 10^\circ]$

Figure 11 shows the convergence of both the lift coefficient and the overall solution. While in the lower angles of attack both cases converged rapidly, at the higher angles of attack there are fluctuations in the lift coefficient value even after many iterations. At 10° AOA, the aircraft is stalled and the flow-field does not converge.



4.3 Rigid vs Elastic Analysis - Euler

All the simulations in this section performed in the altitude of $h=14030.4$ [m], in a dynamic pressure of $q=394.8$ [pa], at Mach number of $M=0.2$, which represents the dynamic pressure at sea-level flight in the velocity of 25 [m/s].

4.3.1 Angle of Attack Comparison

Inviscid Euler analysis at several AOA values were conducted to understand the effect of wing elasticity on the aerodynamic coefficient. The deformed shape

of the wing is represented as combination of modal deformations (Eq. 3). Table 5 presents modal displacements at the first three elastic modes computed at AOA of 0,1,3 and 5 degrees. The largest participation is of the first bending mode. The modal deformation increases with the AOA. Figures 12 and 13 show the rigid and elastically deformed wings at 0° and 5° AOA, respectively. At 5° AOA, the wing tip is twisted nose-up by 3.91°. This contributes to increased local AOA at outboard wing sections and therefor increased lift (aeroelastic efficiency greater than 1).

Table 5: Elastic Modes Participation - ξ

AOA	Mode 1	Mode 2	Mode 3
0°	$-1.498e^{-5}$	$-1.13e^{-4}$	$-4.41e^{-5}$
1°	-0.0013	$5.77e^{-4}$	0.0018
3°	-0.004	0.0019	0.0057
5°	-0.0061	0.0031	0.0094

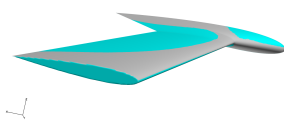


Figure 12: Wing Shape At AOA=0°, Grey-undeformed, Cyan-deformed

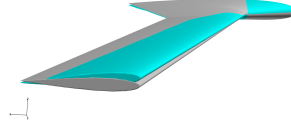


Figure 13: Wing Shape At AOA=5°, Grey-undeformed, Cyan-deformed

At zero AOA the aerodynamic load, and hence the elastic deformation should be zero. Due to a slight asymmetric of the airfoil there are small forces even at zero AOA, which result in slight nose-down pitch and downward bending of the wing. To evaluate the aerodynamic coefficient of each angle of attack, the zero-angle value of the has been subtracted. As expected, with the increase of the angle of attack the elastic configuration generates more lift than the rigid configuration, as seen in figure 14.

In figure 15, the convergence of the lift coefficient is presented. As been mentioned in section 2, an elastic shape update is computed every (approximately) 22% of the total number of iterations which in this case is 500. The elastic convergence trend in figure 15 shows that until convergence is achieved, there is a sharp increase (a jump) at the CL value every 500 iterations, followed by small oscillations while maintaining a converging trend. In both the rigid and elastic cases, the lift coefficient converges - in the rigid configuration after 1500 iteration, and in the elastic configuration after 3000 iterations.

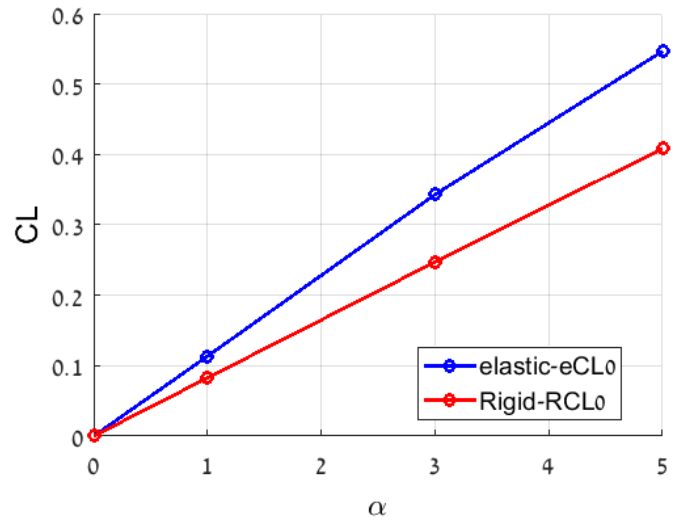


Figure 14: Lift Coefficient versus Angle of Attack, Elastic versus Rigid

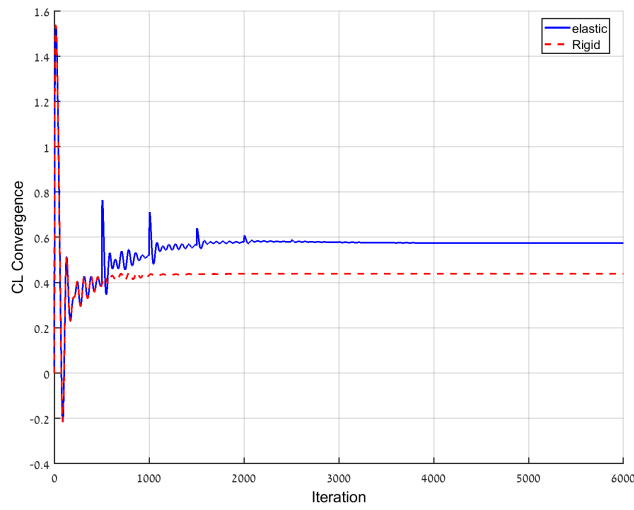


Figure 15: Lift Coefficient Convergence, Elastic versus Rigid, $\alpha = 5^\circ$

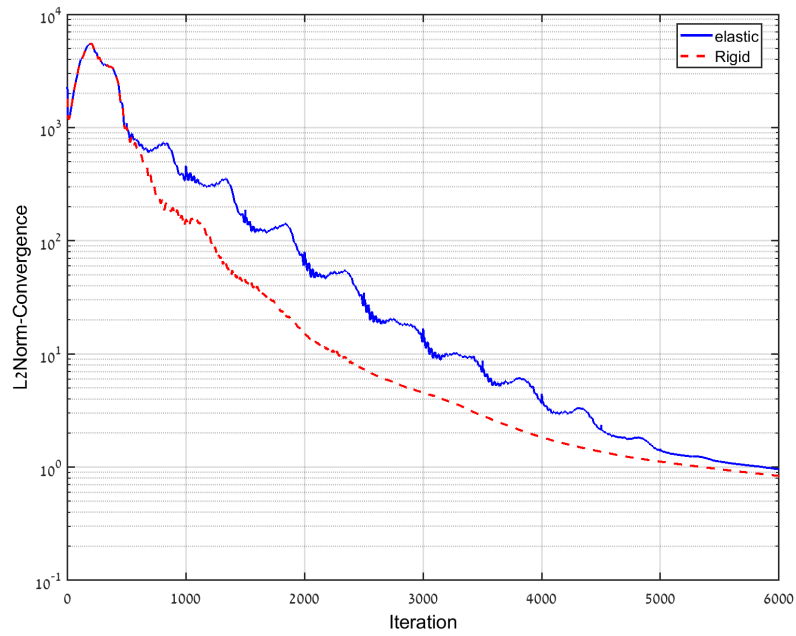


Figure 16: L2Norm Convergence, Elastic versus Rigid, $\alpha = 5^\circ$

Figure 16 shows the L2Norm convergence of the two cases. Until the first aeroelastic correction, both cases have the same behavior. Afterward, we can see the same behavior as in figure 15. After 5000 iterations, both cases have almost the same convergence trend, and after 6000 iterations both cases converged in almost 3 orders of magnitude.

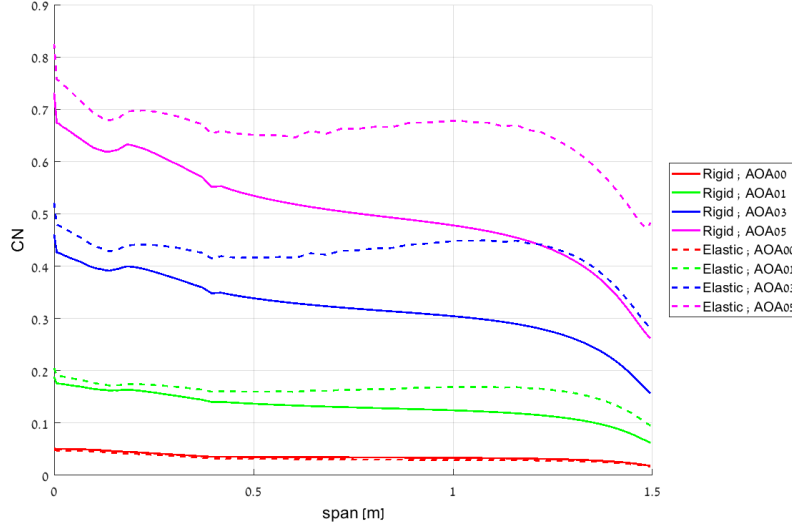


Figure 17: CN Distribution Along Span, Elastic versus Rigid, $\alpha = [0^\circ, 1^\circ, 3^\circ, 5^\circ]$

Figure 17 shows the normal force distribution along the span for the rigid and elastic configurations, in different angles of attack. With increase of the angle of attack, the differences between the rigid and elastic configurations increase as well. In the elastic configuration, due to the nose-up pitch of the loaded wing, more lift is generated in outboard sections. The most significant differences can be found in about 60% – 80% of the span.

4.3.2 Flap Comparison at 0° Angle of Attack

Figure 18 and table 6 show the lift coefficients and slope for each flap, for the rigid and flexible cases.

For both the rigid and elastic configurations, the inboard flap (1) is the most efficient (as indicated by its highest lift slope) and the outboard flap (4) is the least efficient. Besides flap-2, the lift slope curve is higher for the elastic configuration than for the rigid one. Flap 4 is influenced the most from the configurations differences, while flap 2 is influenced the least, with an opposite trend (becoming less effective).

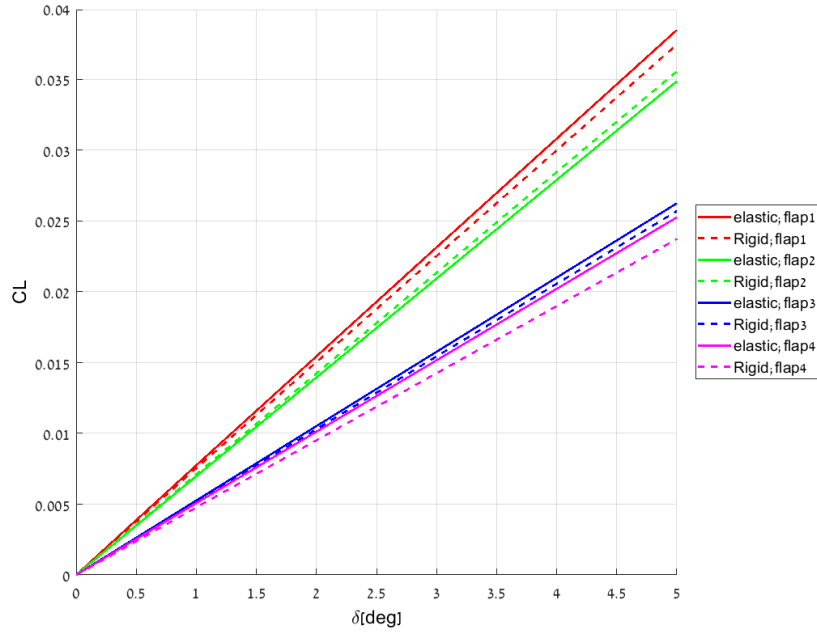


Figure 18: Lift Coefficient versus Angle of Attack, Elastic versus Rigid Flaps Comparison

Table 6: Flaps Lift Slope Curve - CL_δ

Flap	Rigid CL_δ [1/rad]	Elastic CL_δ [1/rad]	η
1	0.4293	0.4411	2.75%
2	0.4077	0.3997	-1.96%
3	0.2945	0.3009	2.17%
4	0.2719	0.2894	6.44%

Moreover, there is a particularly large difference at the lift slope curve, $C_{L\alpha}$ between flaps 1,2 and flaps 3,4.

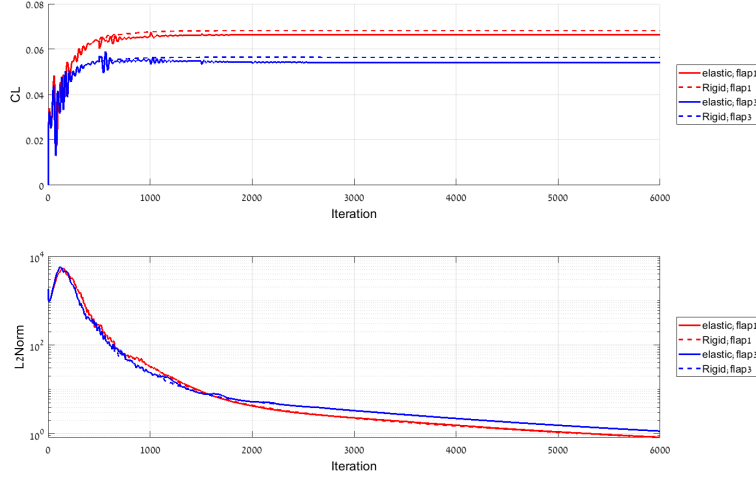


Figure 19: Convergence at $\alpha = 0^\circ, \delta = 5^\circ$, Elastic versus Rigid Flaps 1,4 Comparison

In figure 19 we can see the convergence of both the lift coefficient and the overall solution. Unlike in figures 15 or 16, the fluctuations here are much smaller, due to smaller deformations, which create a smoother convergence line.

Figure 20 shows the normal force coefficient distribution over the span for the four deflected flaps, for the rigid and elastic configurations. In figure 20 we can see that the rigid configuration generates greater normal force along the span than the elastic configuration. The trend of the rigid and elastic spanwise loads is almost identical for the different flaps. Flaps 1,2 achieve almost the same max C_N values, which is higher than the C_N value at flaps 3,4.

Also, there are sharp changes in the values of C_N along the span. These may be due to the combination of the grid density and the process by which the flaps are being deflected.

Flaps efficiency

The efficiency of the flaps, was calculated as follows:

$$\eta_f = \frac{C_{L\delta}^{elastic} - C_{L\delta}^{rigid}}{C_{L\delta}^{rigid}} \cdot 100 \quad (7)$$

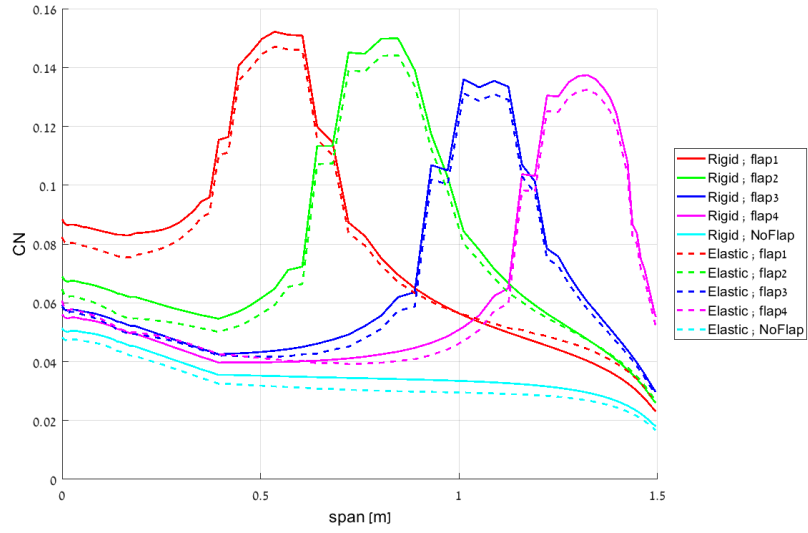


Figure 20: CN Distribution Along Span, Elastic versus Rigid Flaps Comparison at $\alpha = 0^\circ$, $\delta = 5^\circ$

CL	AOA00	ela	Rigid	ela:(flap-NoFlap)	Rigid:(flap-NoFlap)	((ela-Rigid)/Rigid)%
NoFlap	-	2.79E-02	3.07E-02	-	-	-9.30%
flap1	d01	3.56E-02	3.83E-02	7.75E-03	7.55E-03	2.69%
	d03	5.10E-02	5.32E-02	2.32E-02	2.25E-02	2.74%
	d05	6.64E-02	6.82E-02	3.85E-02	3.75E-02	2.74%
flap4	d01	3.29E-02	3.55E-02	5.08E-03	4.78E-03	6.41%
	d03	4.30E-02	4.50E-02	1.52E-02	1.43E-02	6.41%
	d05	5.31E-02	5.44E-02	2.53E-02	2.37E-02	6.44%

Figure 21: Flap Efficiency Comparison at AOA=0

At an angle of attack of 0° , and deflection of flaps 1,4 in angles of $\delta = [1^\circ, 3^\circ, 5^\circ]$, we obtain the efficiency of 2.74% for flap1, and 6.4% for flap4, in favor of elastic configuration.

4.3.3 Flap Comparison at 5° Angle of Attack

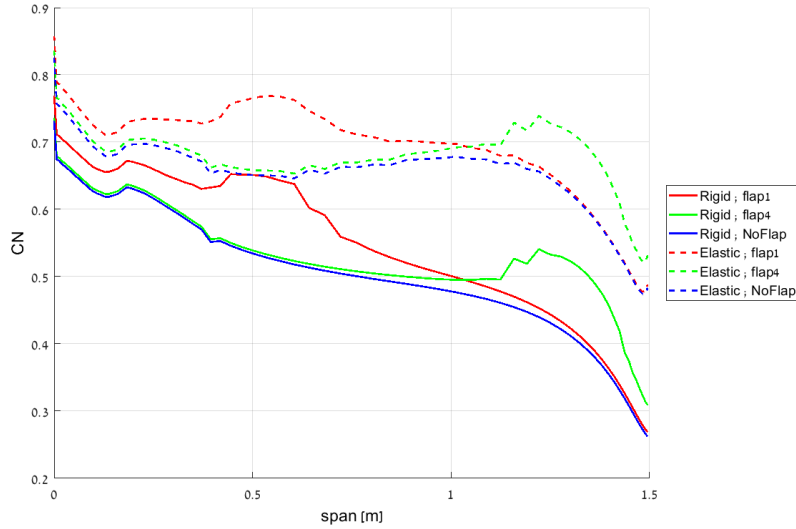


Figure 22: C_N Distribution Along Span, Elastic versus Rigid Flaps 1,4 Comparison at $\alpha = 5^\circ$

Figure 22 shows the normal force coefficient distribution over the span for the four deflected flaps, for the rigid and elastic configurations at 5° AOA. In figure 22 we can see that the differences in values of C_N are mainly because of the angle of attack $\alpha = 5^\circ$, while the contribution of flaps is much lower than the $\alpha = 0^\circ$ case. Moreover, the flaps contribution of the elastic configuration is less than the rigid configuration, as will be specified in the efficiency of the flaps.

Flaps efficiency

Using the same process as used in $\alpha = 0^\circ$, we obtained the efficiency of the flaps for $\alpha = 5^\circ$ for an elastic configuration, in comparison to the rigid one. In this case, when the deflection of the flap is $\delta = 1^\circ$, the efficiency obtained is the lowest for flap 1: -12.6% and is the greatest for flap 4: -6.9% . For deflections of $\delta = [3^\circ, 5^\circ]$, the efficiency of flaps is around -8.5% . It follows, that the flaps lose their efficiency in the elastic configuration, in comparison of the rigid configuration, as expected.

						((ela-Rigid)/Rigid)%
CL	AOA05	ela	Rigid	ela:(flap-NoFlap)	Rigid:(flap-NoFlap)	addition ela vs Rigid
NoFlap	-	5.75E-01	4.39E-01	-	-	30.84%
flap1	d01	5.81E-01	4.46E-01	6.29E-03	7.20E-03	-12.64%
	d03	5.95E-01	4.62E-01	2.08E-02	2.27E-02	-8.41%
	d05	6.10E-01	4.77E-01	3.50E-02	3.82E-02	-8.42%
flap4	d01	5.79E-01	4.44E-01	4.55E-03	4.89E-03	-6.95%
	d03	5.88E-01	4.54E-01	1.36E-02	1.49E-02	-8.62%
	d05	5.97E-01	4.64E-01	2.25E-02	2.47E-02	-8.75%

Figure 23: Flaps Efficiency Comparison at AOA=5

5 Conclusions

This report summarizes results of an aeroelastic investigation of a half flying-wing configuration, using the EZNSS CFD code. Comparing results of the Euler and Navier-Stokes models, we found that due to the low Reynolds number and its effect on the boundary layer's thickness, the Euler-computed lift coefficient is slightly higher than that from the Navier-Stokes. The Euler simulation time is much shorter than Navier-Stokes; Although the Euler model is less accurate, it provides a good approximation of the aerodynamic coefficients for the rigid and deformed configurations, in a short time.

the study examined the effect of wing elasticity on the aerodynamic coefficient, focusing on the lift. From the Navier-Stokes simulations, we found that the stall angle for the elastic configuration is about 8° due to stall of the out-board sections. A positive AOA causes positive wing twist which increases the effective AOA, and as a result, a larger value of lift coefficient obtained in comparison to the rigid configuration. The convergence trend is maintained in both configurations, inspite of small oscillations due to the aeroelastic corrections following every 500 iterations.

Investigation of the deflected flaps shows that with increase of the AOA, the efficiency of the flap of the elastic wing is decreasing. While in 0° AOA there is an improvement of 2-6% at the efficiency of the flaps, in AOA of 5° the rigid configuration efficiency is better by 8%.